Spline-Based 3D-to-2D Image Registration for Image-Guided Surgery and 3D Electron Microscopy

Slavica Jonić[1,2,*], Philippe Thévenaz[2], C. O. S. Sorzano[3], Michael Unser[2]

[1]*IMPMC, Université Pierre & Marie Curie, F-75015 Paris, France*
[2]*Biomedical Imaging Group, Ecole Polytechnique Fédérale de Lausanne, CH-1015 Lausanne, Switzerland*
[3]*Escuela Politécnica Superior, Universidad San Pablo-CEU, 28668 Boadilla del Monte, Madrid, Spain*
[*]*Correspondence: Slavica.Jonic@impmc.jussieu.fr*

Abstract: This paper focuses on techniques for rigid-body registration of a Three-Dimensional (3D) model to a set of Two-Dimensional (2D) x-ray images in Computer-Assisted Orthopedic Surgery (CAOS) and in 3D Electron Microscopy (3D EM). In the first part of the paper, we present a survey of these techniques. In the second part, we describe our strategy for solution of these two problems. Our algorithm relies on a space-based iterative minimization of the least-squares dissimilarity between the x-ray images and their simulations. To allow for a well-defined gradient of the dissimilarity measure when simulating the x-ray images, we use cubic B-splines for interpolation of the volume. We improve the robustness of the algorithm thanks to the multiresolution data pyramids that we compute using cubic B-splines too. In the third part, we show the performance of our algorithm using phantom CAOS and EM data with the ground-truth registration that is known *a priori*.

1. INTRODUCTION

The registration of two sets of points assumes two steps: 1) determination of a geometric transformation between the sets, and 2) application of the transformation to one of them to align it with the other. The most general transformation between the sets is elastic, which means that a straight line is mapped onto a curve. If the transformation preserves the distance between any two points, it is called a rigid-body transformation. The need for registration exists in many fields like medicine, biology, manufacture, robotics, computer vision, computer graphics etc. [1-5].

Our work is focused on the techniques for registration of Two-Dimensional (2D) images of a subject to its Three-Dimensional (3D)

representation. We consider the application of these techniques in medicine and biology. These images may be acquired at different times, from different sensors, from different viewpoints, or from different subjects [6-8]. In this paper, we present our algorithm for 3D-to-2D image registration and its potential application in Computer-Assisted Orthopedic Surgery (CAOS) [9-10] and in 3D Electron Microscopy (3D EM) [11].

1.1 Intuitive 3D-to-2D registration

Let us imagine a sunny day. We are in a room with a window and a desk is placed along a wall. The desk makes a shadow on the wall. Let us now imagine that someone cleaning the room has moved the desk to some other place but its shadow on the wall has been captured by some means. We may be assigned the following task: Return the desk to its original position by matching its actual shadow to the captured one. Obviously, to make it, we have to come the next day at the same time at which the shadow has been captured the day before, that is, when there is the same sunlight in the room. The positioning of the desk, by matching its reference and current shadows, is an illustration of what we are doing when performing the 3D-to-2D image registration. In this case, we would return the desk in a few simple movements, that is, we would only have to shift it and/or to turn it. In a more complicated case, for instance, of having to position a cat (instead of a desk) by shadow matching, we would have to account for more complex, free movements of the cat. In the case of the desk, we would therefore perform a rigid-body registration of the desk to its reference shadow while, in the case of the cat, we would have to perform an elastic registration of the cat to her reference shadow.

We will now consider two applications of 3D-to-2D image registration where we have access to more than just shadows. By replacing sunshine by x-rays, we will have access to the interior of the objects; this will make for richer, but more challenging data.

1.2 Registration requirements of CAOS and of 3D EM

One of the requirements of CAOS is an intraoperative visualization of the position of surgical tools in preoperative 3D Computed Tomography (CT) patient data. To achieve this, one registers

the CT to a set of intraoperatively acquired cone-beam x-ray images of the patient (Figure 1) [12-23]. The registration accuracy is mainly limited by the following six factors: 1) few images (less than five) because of a limited radiation to which the staff and the patient are exposed, 2) limited field of view, 3) tools that are visible in the images, 4) limited data resolution (in particular, that of the CT volume), 5) accuracy of the registration algorithm, 6) movements of the patient.

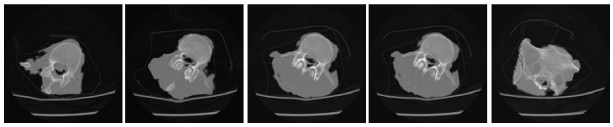

(a)

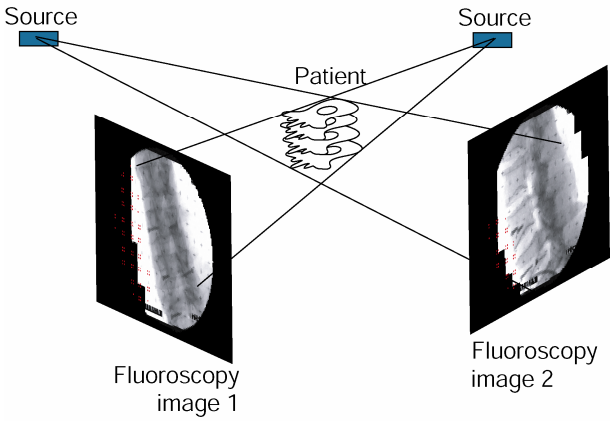

(b)

Figure 1: Application of the 3D-to-2D image registration in image-guided orthopedic surgery. A 3D CT of a patient (a) is aligned to his fluoroscopy (x-ray) images (b) to allow display of the position of surgical tools in the CT during the intervention.

3D EM yields a 3D model from a set of x-ray parallel-beam images of single particles (Figure 2). The orientation of these images is unknown and has to be estimated before applying an algorithm for 3D reconstruction [24-25]. Given an earlier 3D reconstruction, the 3D-to-2D image registration can be used to refine these estimates [26-41]. A new 3D reconstruction based on a better estimate of these orientations should improve on the previous one. Contrary to the CT-to-x-ray image registration, one can collect thousands of images for 3D EM but they

suffer from a very low signal-to-noise ratio. An additional difficulty is an image distortion due to the Contrast Transfer Function (CTF) of the electron microscope. This makes the image differ from the theoretical parallel-beam projection and this problem often difficult to solve at sub-nanometer resolutions.

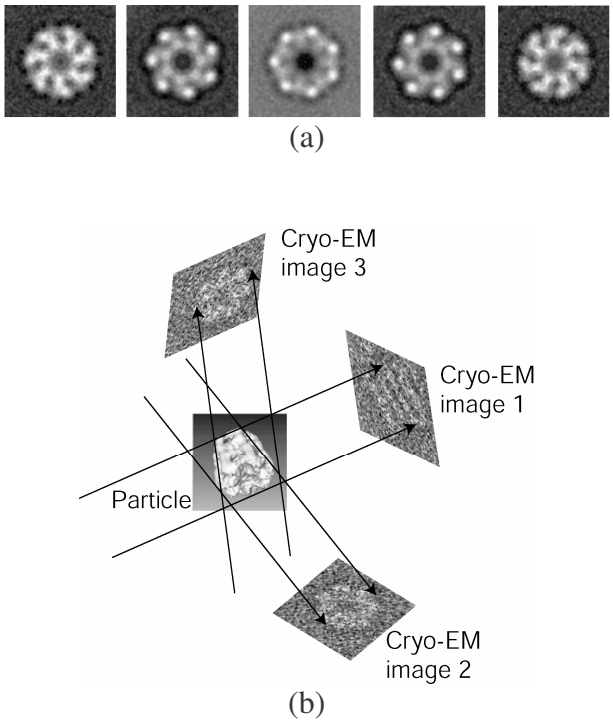

Figure 2: Application of the 3D-to-2D image registration in 3D electron microscopy. A 3D model of a protein (a) is aligned to its Cryo-Electron Microscopy (Cryo-EM) images (b) for refinement of their orientation such that a more accurate 3D model of the protein can be reconstructed.

2. STATE OF THE ART

We can classify existing 3D-to-2D image registration algorithms in two groups. The first group of algorithms is based on matching features that have first to be extracted from both the volume and the images. They match either markers (artificial features) implanted onto the subject prior to data acquisition [9], or anatomical features [12-14,16,21-22,42]. The

registration based on artificial markers is not enthusiastically accepted for medical applications because of its invasiveness.

The registration based on anatomical features requires an accurate segmentation, which is difficult to achieve fully automatically. It takes advantage of an extension of the standard fast iterative closest point algorithm for registration of curves and surfaces. However, the time required for accurate segmentation makes it unattractive for surgical interventions. An additional disadvantage is a low robustness against a partial data problem (presence of a feature in one imaging modality and its absence in the other).

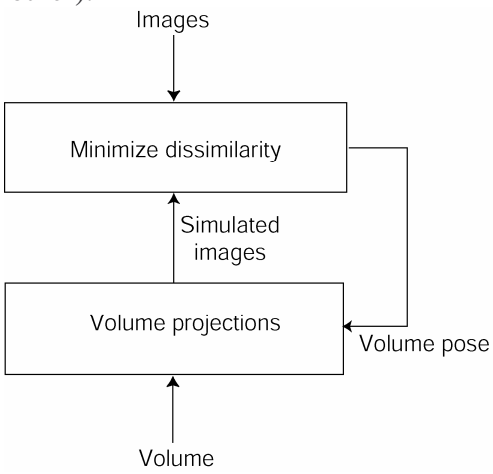

Figure 3: Diagram of the projection-based 3D-to-2D registration methods.

Neither of the two approaches can be applied for electron-microscopy data registration since the true 3D model is not known; Feature extraction makes therefore no sense there. Fortunately, the second group of methods, projection-based methods [15,17-20,27-28,33,37,39,40-41,43-44], can be used in 3D EM since they do not require feature extraction. These methods achieve the registration by matching a set of images to their simulations (Figure 3). The simulations are traditionally computed by integrating the volume intensities along simulated x-rays through the volume (Figure 4). The matching is done by minimizing a measure of dissimilarity between the images and their simulations using an iterative refinement of an initial estimate for the unknown parameters. Thus, the robustness of these methods depends on the quality of the estimate. When close to the solution initially, they promise a high accuracy because of use of a large amount of data.

However, their speed decreases with an increase in data size. Some of these methods perform the registration in the Fourier space based on the central-slice theorem [27-28,37,41]. These methods are perfectly suited to 3D EM because of its parallel-beam projection geometry. More general are the methods that perform the registration in real space since they can be adapted to cone-beam or parallel-beam geometry depending on the application. In this paper, we present a real-space projection-based algorithm that satisfies this requirement and could therefore be applied in both 3D EM and CAOS.

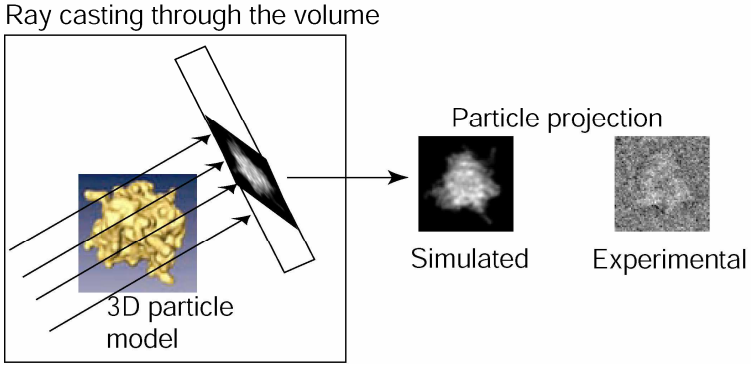

Figure 4: Simulation of an experimental image of a protein by casting the simulated x-rays through its 3D model.

To simulate the acquired images, the projection-based methods require a 3D interpolation of the given volume. Given some equidistant samples of a function, the ideal reconstruction kernel is the sinc function. However, this function is not acceptable in practice due to its slow decay. Thus, it is traditionally replaced by some approximation with faster decay (optimal Keys' cubic interpolant, the triangle function for the linear interpolation, and the rectangular pulse for the nearest-neighbor interpolation) [45].

The ray casting is usually done using tri-linear interpolation [43-44]. In our method, the registration process is driven by the gradient of the dissimilarity measure. To get the gradient well defined everywhere, we use B-splines for the volume interpolation [46-47]. We select the spline degree such that we achieve a good tradeoff between the computational speed and interpolation quality. Traditionally, we use B-splines of degree 3 (cubic B-splines).

Different methods have been used to minimize the selected measure of dissimilarity [48] such as exhaustive-search techniques

[33,39], Powell's multidimensional direction-set method [37,43-44], gradient-descent-type search techniques [18], and a quasi-Newton algorithm [40]. To make the first derivative of the measure of dissimilarity easy to compute analytically, we have chosen to use a least-squares dissimilarity measure. Besides, least-squares criterions are known to be good for data fitting (parameter identification), which is our case since we match the input images to their respective models. To make the registration fast, we employ a Levenberg-Marquardt (LM) [49] algorithm to minimize the dissimilarity measure as described in [41].

The 3D-to-2D image registration for CAOS is commonly done within a space of continuous values of geometrical parameters [15,18,20]. However, in 3D EM, a great number of images is usually processed. To reduce the time required for processing of all particle images in a first phase of the 3D model refinement, one commonly does the search within a space of quantized geometrical parameters [33-34,39]. These methods are in general based on building a discrete set (library) of volume projections that are evenly distributed in space, and on matching of the captured images to the library. The quantization step is reduced gradually in the repeated refinement cycles. In the final stage, one performs a refinement of continuous values of the parameters in the Fourier domain [37,41]. Yang *et al*. [40] propose the continuous refinement of the parameters in real space but with a simultaneous refinement of the 3D model. A similar strategy for the search of the geometrical parameters and a simultaneous 3D reconstruction in the Fourier domain has been promoted by Provencher and Vogel [27-28]. These methods optimize a large number of parameters, which means a higher risk for the algorithms to get trapped into local optima of the cost function, and an augmented dependence on the quality of the starting estimates for the parameters. Our algorithm performs the refinement of continuous values of the geometrical parameters. To allow for the application of our algorithm in both CAOS and 3D EM, we separate the parameter refinement from the 3D reconstruction.

The registration is often performed iteratively at multiple data resolutions. The coarse-to-fine data processing is a standard tool for improving the robustness of optimization algorithms. The data at coarser resolutions are smoothed versions of the data at full resolution. The registration using data with no or just a few details augments the chances of reaching the global optimum instead of getting trapped on the way into a local one. Data of a lower resolution are usually obtained by blurring,

using an averaging filter, and by their subsequent subsampling [15,44,48]. In [44], a multiresolution pyramid of the volume was not computed explicitly but the projections of a lower resolution were computed by simply reducing the sampling rate along each ray through the volume, which introduces aliasing. A multiresolution pyramid of a region of interest extracted from the images and from the volume has been used in [48] and [15]. The method proposed in [39] computes the similarity between the images and the library of volume projections based on their wavelet transforms.

The strategies that are based on reducing the data size speed up the optimization. The cost of the iterations at some coarse data resolution is negligible since there is few data to process, and it increases towards finer resolutions. Consequently, one can afford a lot of iterations at coarse resolutions but only few of them at finer ones. This means that the total time required to achieve the registration in a multiresolution fashion is much shorter than required for the registration at full resolution. We use L_2 spline multiresolution volume/image pyramids to make our algorithm more robust as well as faster [50].

3. SPLINE PROJECTION-BASED ALGORITHM

In this section, we describe main building bricks of our algorithm.

3.1 Projection

We simulate a set of captured x-ray images by computing projections of the volume. We define the orientation and the position of the volume in the Reference Coordinate System (R-COS) by three rotations and three translations of the volume. Let $\boldsymbol{\mu} = (\mu_1, \mu_2, ..., \mu_6)$ be a vector of these geometrical parameters. We compute the projections by simulating x-rays through the volume. Given a volume f with the geometrical parameters $\boldsymbol{\mu}$ in the R-COS, we cast the simulated x-rays through each pixel of the image plane. We project the volume along a ray on the pixel with the coordinate $\mathbf{k} = (k_1, k_2, 1)$ as

$$p_{\boldsymbol{\mu}}(\mathbf{k}) = \int_R f(\mathbf{a}_{\boldsymbol{\mu}} + \xi\, \mathbf{b}_{\boldsymbol{\mu}})\, \mathrm{d}\xi .$$

A direct implementation of this equation would require a 3D interpolation of the volume f at the coordinate $\mathbf{a}_{\mu} + \xi\, \mathbf{b}_{\mu}$. We perform a fast computation of the projection by replacing the 3D interpolation by a 2D interpolation as described in [51]. To interpolate the data, we use the B-spline data model that we present below.

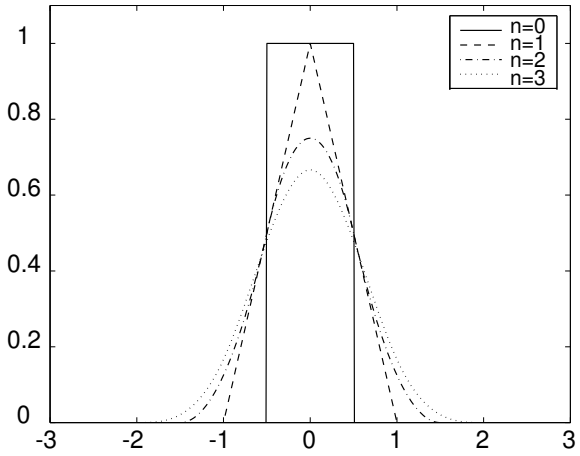

Figure 5: Centered B-splines of degree n=0,1,2, and 3.

3.2 B-spline data model

The B-spline model of a function f reconstructed from its samples $f(\mathbf{k}), \mathbf{k} = (k_1, k_2, ..., k_N) \in Z^N$ is given by

$$f(\mathbf{x}) = \sum_{\mathbf{k} \in Z^N} c_{\mathbf{k}}\, \beta^n(\mathbf{x} - \mathbf{k}), \forall \mathbf{x} = (x_1, x_2, ..., x_N) \in R^N,$$

where the coefficients $c_{\mathbf{k}}$ are obtained by recursive digital filtering [47] of the samples $f(\mathbf{k})$, and where $\beta^n(\mathbf{x})$ is the separable N-dimensional B-spline of degree n given by

$$\beta^n(\mathbf{x}) = \prod_{j=1}^{N} \beta^n(x_j),$$

where $\beta^n(\cdot)$ denotes the centered B-spline of degree n [46] (Figure 5). The separability makes possible an operation on N-dimensional data to be performed by a successive processing of one-dimensional data along

each of the N dimensions. In return, the data processing is simple and fast.

The B-splines have many interesting properties. For instance, the approximation order (and the support) of a B-spline of degree n is equal to $n+1$ [45]. They are shown to be maximally continuous basis functions, with the minimal support for a given order of approximation, and with the maximal order of approximation for a given support [52].

3.3 Solution of the optimization problem

We compute the orientation and the position of the volume $\boldsymbol{\mu}$ with respect to the acquired x-ray images by minimizing a real-valued cost function S that is a function of six variables $\mu_i, i = 1, 2, ..., 6$. We solve the registration problem as a nonlinear least-squares problem, that is, we minimize the function

$$S(\boldsymbol{\mu}) = \frac{1}{2} \sum_{q=1}^{Q} \left(\mathbf{r}_q(\boldsymbol{\mu})\right)^H \mathbf{r}_q(\boldsymbol{\mu}),$$

where $\mathbf{r}_q$ is a difference between the normalized (mean=0, standard deviation=1) $q-\text{th}$ x-ray image and its simulation (the projection of the volume at orientation $\boldsymbol{\mu}$) that are both expressed in a vector form, Q is the number of acquired images, and where $\mathbf{r}^H$ denotes the Hermitian transpose of $\mathbf{r}$. The spline data model (Section 3.2) makes the cost function smooth and makes the exact computation of the gradients possible.

We apply the LM algorithm to minimize the cost function. This is a Newton-like method that is used with least-squares cost functions; in this case, a specific approximation of the Hessian leads to very good convergence properties of the method [41,49].

3.4 Multiresolution strategy

Given a volume and a set of images, we propose to pre-compute their spline L_2 pyramids [50]. We register the volume to the images starting from their coarsest resolution. We use the final estimate obtained at some pyramid level to resume the registration at the next finer one. We repeat

the registration procedure at finer resolutions until we reach a resolution that provides a good tradeoff between accuracy and time [53].

3.5 Measure of misregistration

We transform every volume coordinate $\mathbf{n}$ from the Voxel Coordinate System (V-COS) into the R-COS by using two transformations: the ground-truth transformation B and the transformation $B_{\boldsymbol{\mu}}$ that we estimate using our algorithm. We define the misregistration as the average of the norm of the difference between the two R-COS coordinates over all V-COS indexes $\mathbf{n}$, that is,

$$\varpi = \frac{1}{\mathrm{card}(f)} \sum_{\mathbf{n} \in f} \left\| \left(B - B_{\boldsymbol{\mu}} \right) \mathbf{n} \right\|.$$

In case of perfect registration, which is achieved when $B_{\boldsymbol{\mu}} = B$, we have that $\varpi = 0$. Note that this measure is expressed in voxel units but takes into account both angular and translational assignment accuracy.

4. REGISTRATION OF A 3D CT TO C-ARM IMAGES

In this section, we show the performance of our algorithm when registering the CT volume to a set of C-arm images of a cadaver spine. Here, we determined the ground-truth registration using fiducial markers.

4.1 CT/C-arm data

The data were provided by M.E. Müller Institute for Biomechanics, Bern, Switzerland. A human cadaver spine specimen was frozen so that it can be treated as a truly rigid body. This gives us the opportunity to jointly consider more data (three vertebræ) than is available in clinical practice where each vertebra can exhibit independent motion, thus providing an upper bound to the performance of our registration method. Meanwhile, we can also restrict the focus of our experiments on a single vertebra to obtain results that are indicative of the performance of our method in practice. Five fiducial markers (custom-made, Titanium) were implanted on the spine. One was placed in the L5, two in the L4, and two in the L3 vertebra.

The specimen, placed in a plastic bag that is apparent in the transversal and sagittal views of Figure 6, was CT-scanned (GE LightSpeed Ultra CT scanner) with seventy-two slices of size 512x512, in pixel units. The intra-slice pixel size was 0.36x0.36, in mm units, and the inter-slice thickness was 2.5 mm. The tilt angle was zero.

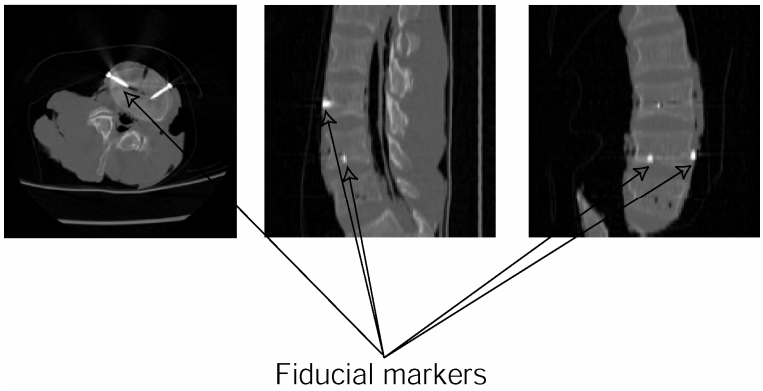

Figure 6: CT with visible fiducial markers. Transversal (left), sagittal (center), and frontal (right) CT slices.

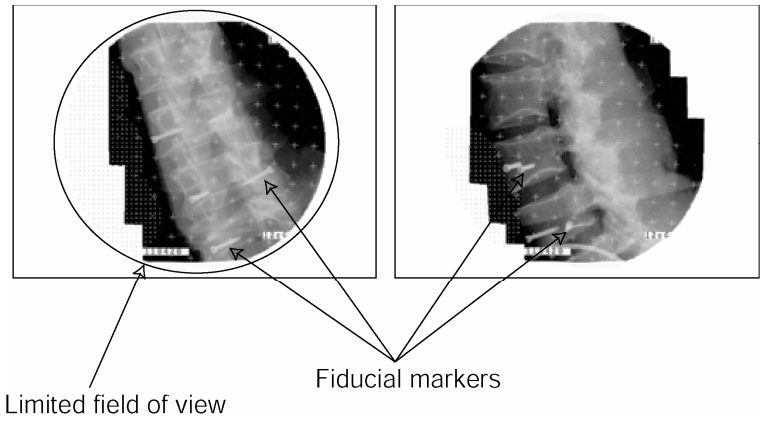

Figure 7: C-arm images with visible fiducial markers and a superimposed grid of crosses used to un-warp the images in a calibration step.

The images were acquired using a Siemens ISO-C C-arm instrumented with LED markers. Their positions were tracked using an optoelectronic position sensor (Northern Digital Optotrak 3020). The geometric parameters of the C-arm x-ray image (the orientation and the position of the image plane as well as the position of the illumination source) were determined according to the two-step procedure proposed

by Hofstetter *et al*. [54]. The optical tracking system and the calibration procedure resulted in the navigation error being 0.5±0.5 mm [54]. The captured images were un-distorted before further use [54]. We display two of them in Figure 7 and their simulations that were computed using our algorithm in Figure 8. The images were of size 768x576, in pixel units, and the pixel size was 0.36x0.36, in mm units.

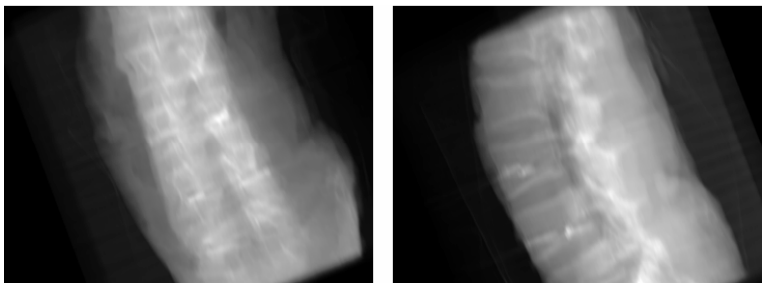

Figure 8: Simulated C-arm images from Figure 7.

Typical clinical settings involve a device called a Dynamic Reference Base (DRB) to define the Patient Coordinate System (P-COS) in which the tools are tracked. In spinal surgery, the DRB is commonly clamped to one of the vertebræ; Both DRB and clamp are therefore visible in the C-arm images. Their presence challenges our registration algorithm because neither DRB nor clamp is present in the CT data. Two of these images are presented in Figure 9.

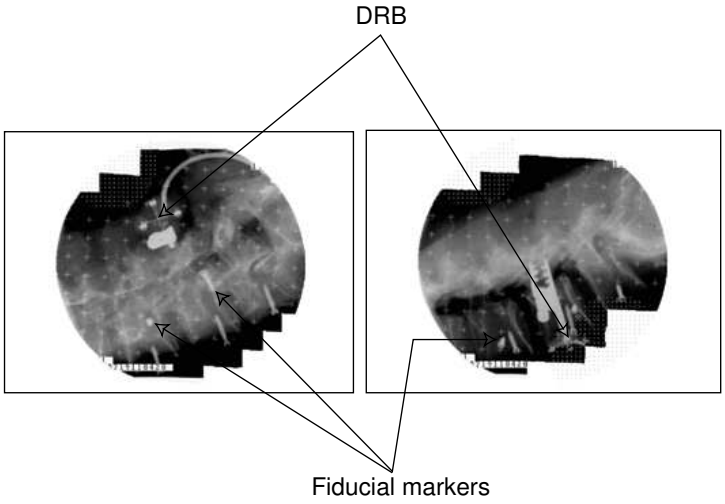

Figure 9: C-arm images with a visible Dynamic Reference Base (DRB).

To determine the ground-truth registration, the coordinates of the fiducial markers were digitized in the P-COS using an optoelectronically tracked (Northern Digital Optotrak 3020) pointer. Then, they were transformed into the R-COS. The coordinates of the fiducial markers in the V-COS were estimated by fitting a sphere to the marker heads.

4.2 Ground-truth transformation

To measure the registration accuracy, we replace B in the measure of misregistration ϖ (Section 3.5) by the transformation estimated using a given list of coordinates of the fiducial markers in the R-COS ($\mathbf{v}_i, i = 1, ..., 5$) and in the V-COS ($\mathbf{n}_i, i = 1, ..., 5$). The estimation of B is done by minimizing $\chi^2 = \frac{1}{5}\sum_{i=1}^{5} \| \mathbf{v}_i - B\,\mathbf{n}_i \|^2$ in terms of B.

4.3 Multiresolution

We use four-level dyadic CT-volume and C-arm-image pyramids. These pyramids are dyadic in only two directions; we do not change the number of CT slices while performing the data reduction. We perform the registration at the two coarsest pyramid levels only, since this strategy gives a good tradeoff between accuracy and time. We have found that we do not gain more than 0.2 mm accuracy if we perform additional processing at the two finest data resolutions. This does not justify the huge additional registration time. We could have coarsened the data further, for example by computing five-level pyramids, or by reducing the number of CT slices. However, such pyramids do not improve the performance of our algorithm since they result in either failures at the coarser data resolutions, or fail to perform better at finer data resolutions.

4.4 Performance

We have found that our algorithm operates successfully if the angle between at least two image planes is larger than some threshold that depends on the amount of available data. When sufficient data are available (three vertebræ), this threshold is 10º. In more-demanding clinical conditions (single vertebra), it is 25º. Also, we have found that the registration accuracy could be improved by increasing the number of C-arm images. Moreover, we found that a good tradeoff between the

radiation dosage, the registration accuracy, and the registration time, could be achieved with three different C-arm orientations. When registering the CT volume to triplets of C-arm images, the accuracy of our algorithm is 1.4±0.2 mm for a joint registration of all three vertebræ, and 1.7±0.3 mm for a registration of a single vertebra at a time. In the literature on the 3D-to-2D registration of CT volumes to fluoroscopy images, a registration is commonly treated as successful if some measure of misregistration is below 2 mm [21-22], which is clearly our case.

The residual misalignment can be explained by the fact that some errors were made when digitizing the fiducial markers (the mean navigation error was 0.5 mm), and that some more errors were made when determining the CT indexes of the markers. An independent analysis has shown that the maximum error committed when determining the CT indexes of the markers was about 0.6 mm (25% slice off). This means that, in the experiments carried out, our algorithm is perhaps responsible for a lesser misregistration than that reported. Note that the mean misregistration of 1.4 mm (three vertebræ) and of 1.7 mm (single vertebra) is clearly subvoxel with respect to the inter-slice CT thickness of 2.5 mm.

5. REGISTRATION OF A 3D MODEL OF A PROTEIN TO ITS CRYO-EM IMAGES

In this section, we apply our algorithm to the registration of a 3D model of a protein from the Protein Data Bank (PDB) (http://www.rcsb.org/pdb/) to synthesized cryo-EM images of this protein. These images have a known ground-truth alignment with respect to the 3D model of the protein, which allows for an objective evaluation of the performance of our algorithm.

We test our algorithm using two sets of experiments. The first one shows the robustness of the algorithm to a random value for the initial assignment. The other set of experiments tests the ability of the algorithm to refine an assignment obtained using the wavelet-projection matching [39], a method that is implemented in the Xmipp image processing package for EM. In all the experiments, we run our algorithm using three-level dyadic volume and image pyramids. To measure the accuracy of the assignments, we use the measure of misregistration (Section 3.5) that we adapt to symmetrical particles as described in [41].

5.1 Data

We used a 3D model of the Bacteriorhodopsin from the PDB (accession code: 1BRD [55]). The size of the volume was 64x64x64 voxel and its sampling rate was 3.27Å (Figure 10). The Bacteriorhodopsin found in Halobacterium halobium is a membrane protein that functions as a light-driven pump of protons across the cell membrane. The proton gradient is used by a second membrane protein called ATP synthese to generate metabolic energy in the form of ATP, which is used by the cell to drive many vital processes. When crystallized, the Bacteriorhodopsin forms hexagonal 2D crystals. They are sufficiently well ordered for determining a 3D structure at near-atomic resolution using high-resolution cryo-EM [55]. This protein has a threefold rotational symmetry.

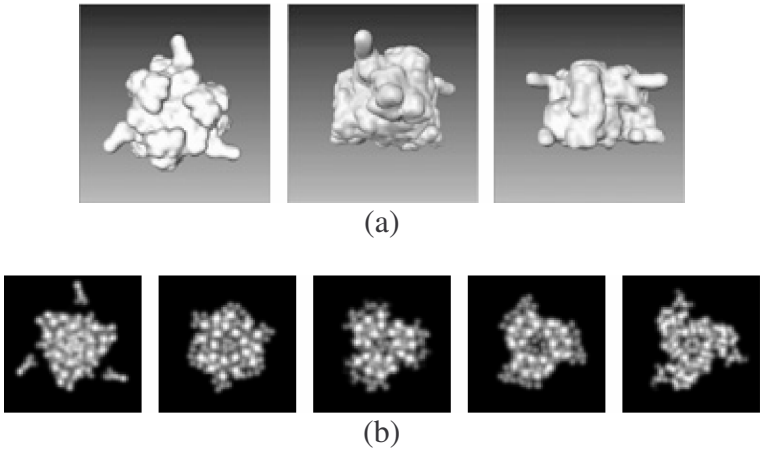

Figure 10: 3D model of the Bacteriorhodopsin from the PDB. (a) Three views of an isosurface. (b) A few slices of the 3D model.

The synthetic cryo-EM images of the Bacteriorhodopsin were computed in a two-step procedure as in [39,41]. In a first step, 1000 projections of the reference model were computed with random orientations. In a second step, noise was added and the CTF was applied using a model proposed by Velázquez-Muriel *et al*. [56]. The synthesized images were of size 64x64 pixel. A few examples of these random projections and of the corresponding synthesized cryo-EM images are shown in Figure 11.

5.2 Robustness

We designed four experiments to test the robustness of our algorithm on the initial assignment. In the first experiment, we initialized the parameters by their ground-truth values. In the second experiment, we initialized the angles by their ground-truth values modified by 5º or -5º with probability 0.5. The initial values for the translation parameters were equal to their ground-truth values. In the third and fourth experiments, the angular perturbation was ±10º and ±15º, respectively.

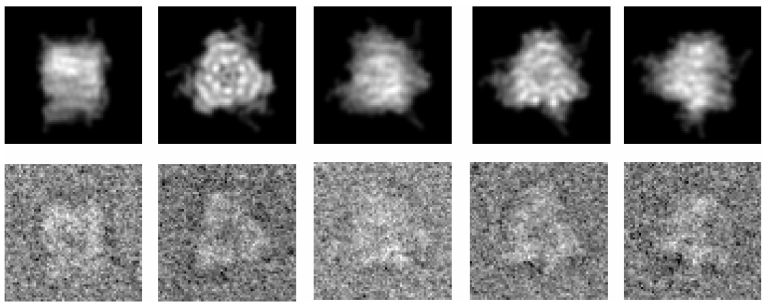

Figure 11: Projections of the 3D model of the Bacteriorhodopsin (first row) and the corresponding synthesized cryo-EM images (second row).

Starting from the ground-truth assignment, the algorithm converged to an assignment that was not the ground-truth one (misregistration of 1.25±0.58 voxel). This can be attributed to the presence of noise and to the CTF, which make a synthetic cryo-EM image differ from the corresponding theoretical projection. For the angular perturbation of ±5º (the initial misregistration of 3.55±0.89 voxel), our method achieved the registration with an accuracy of 1.89±0.77 voxel. In the two remaining cases, ±10º (the initial misregistration of 7.10±1.76 voxel) and ±15º (the initial misregistration of 10.55±2.61 voxel), the registration was accomplished with an accuracy of 4.30±2.22 voxel and 7.86±3.93 voxel, respectively.

5.3 Refinement of a standard-method assignment

We initialized our algorithm using the assignment by the wavelet-projection matching [39] since it showed the best performance when compared with two other quantized-parameter algorithms [41]. This

initial assignment meant an initial misregistration of 3.18±1.85 voxel, which was reduced by our algorithm to 2.23±1.54 voxel.

6. Conclusion

We have developed an algorithm for registration of a volumetric image to a set of given 2D x-ray images. The algorithm performs the registration in the space domain. It relies on an iterative minimization of the least-squares difference between the given and simulated projections of the volume. To simulate the x-ray images, our algorithm uses cubic B-splines for interpolation of the volume. This allows for a well-defined gradient of the dissimilarity measure, which is a necessary condition for efficient and accurate registration. To get a consistent approach, we also use the cubic B-splines to compute the multiresolution volume and image pyramids. The multiresolution improves the robustness of the algorithm. To speed-up the simulation of the x-ray images, we use a one-step approach for fast ray casting that requires mere 2D interpolation instead of the more costly 3D interpolation.

We have adapted our algorithm to the perspective projection model, sometimes called a cone-beam projection. This allows for its application to the registration of a CT volume to a set of C-arm images of a patient for Computer-Assisted Orthopedic Surgery (CAOS). For the data set that we used here, our algorithm achieves the accuracy of 1.7±0.3 mm when registering a single vertebra at a time based on triplets of C-arm images that meet at an angle greater than 25º. The achieved accuracy is subvoxel with respect to the CT that has an inter-slice thickness of 2.5 mm.

We have also adapted our registration algorithm to the parallel-beam projection model such that it can be used for a 3D reconstruction of a protein from its 2D cryo-Electron Microscopy (cryo-EM) images. In the robustness experiments with synthetic Bacteriorhodopsin data, we found that our algorithm reduces each of the three tested initial random angular misalignments (±5º,±10º, and ±15º). This reduction is about 45% for the initial misalignment of ±5º, and it decreases to about 25% for the initial misalignment of ±15º. In terms of our measure of misregistration, the misalignment of ±5º corresponds to about 3.5 voxel while the misalignment of ±15º corresponds to about 10.5 voxel. Our algorithm can be used to refine the alignment obtained by standard quantized-parameter

methods. In the experiments described here, it improves the initial registration achieved by the wavelet-projection matching by about 30%.

These results are promising and require further tests of our algorithm using more sets of CAOS and cryo-EM data, including real data sets.

ACKNOWLEDGMENTS

This work was supported in part by grant 02-U61 from the AO ASIF Foundation, Switzerland, and in part by the Swiss National Science Foundation under grant 2153-066938.01/1.

REFERENCES

1. Bajura M., Neumann U., *IEEE Computer Graphics and Applications*, **1995**, *15*, 52.
2. Bispo E. M., Fisher R. B., *in The Mathematics of Surfaces VI*, G. Mullineux, ed., Oxford Clarendon Press, **1996**, 119.
3. Meilhac C., Nastar C., *in Proc. ICIAP'97*, A. Del-Bimbo, ed., **1997**, *1*, 661.
4. Meyer S. A., Wolf P. D., *IEEE Trans. Biomed. Eng*., **1999**, *46*, 1471.
5. Rueckert D., Sonoda L. I., Hayes C., Hill D. L. G., Leach M. O., Hawkes D. J., *IEEE Trans. Med. Imag*., **1999**, *18*, 712.
6. Brown L. G., *ACM Computing Surveys*, **1992**, *24*, 325.
7. van den Elsen P. A., Pol E. -J. D., Viergever M. A., *IEEE Engineering in Medicine and Biology Magazine*, **1993**, *12*, 26.
8. Hawkes D. J., *in Medical Image Registration*, J. V. Hajnal, D. L. G. Hill, and D. J. Hawkes, eds., CRC Press LLC, Boca Raton, Florida, **2001**, 11.
9. Bainville E., Bricault I., Cinquin P., Lavallée S., *in Computer Assisted Orthopedic Surgery (CAOS)*, L.P. Nolte and R. Ganz, eds., Hogrefe & Huber Publishers, Seattle-Toronto-Bern-Göttingen, **1999**, 15.
10. Edwards P. J., Hawkes D. J., Penney G. P., Clarkson M. J., *in Medical Image Registration*, J. V. Hajnal, D. L. G. Hill, and D. J. Hawkes, eds., CRC Press LLC, Boca Raton, Florida, **2001**, 253.
11. Frank J., *Three-Dimensional Electron Microscopy of Macromolecular Assemblies*, Academic Press, **1996**.

12. Hamadeh A., Sautot P., Lavallée S., Cinquin P., *in Proc. Med. Robot. Comput.-Assisted Surgery (MRCAS'95),* **1995**, 39.
13. Lavallée S., Szeliski R., *IEEE Trans. Pattern Anal. Machine Intell.*, **1995**, *17*, 378.
14. Feldmar J., Ayache N., Betting F., Comput. Vision Image Understanding, **1997**, *65*, 403.
15. Weese J., Penney G. P., Desmedt P., Buzug T. M., Hill D. L. G., Hawkes D. J., *IEEE Trans. Inform. Technol. Biomedicine*, **1997**, *1*, 284.
16. Guéziec A., Kazanzides P., Williamson B., Taylor R. H, *IEEE Trans. Med. Imag.,* **1998**, *17*, 715.
17. LaRose D., Bayouth J., Kanade T., *in Proc. SPIE. Medical Imaging 2000: Image Processing*, K. M. Hanson, ed., **2000**, *3979*, 385.
18. Penney G. P., Batchelor P. G., Hill D. L. G., Hawkes D. J., Weese J., *Med. Phys.*, **2001**, *28*, 1024.
19. Rohlfing T., Russakoff D. B., Murphy M. J., Maurer C. R., *in Proc. SPIE. Medical Imaging 2002: Image Processing*, M. Sonka and J. M. Fitzpatrick, eds., **2002**, *4684*, 581.
20. Birkfellner W., Wirth J., Burgstaller W., Baumann B., Staedele H., Hammer B., Gellrich N. C., Jacob A. L., Regazzoni P., Messmer P., *Phys. Med. Biol.*, **2003**, *48*, 2665.
21. Livyatan H., Yaniv Z., Joskowicz L., *IEEE Trans. Med. Imaging*, **2003**, *22*, 1395.
22. Tomaževič D., Likar B., Slivnik T., Pernuš F., *IEEE Trans. Med. Imaging*, **2003**, *22*, 1407.
23. van de Kraats E. B., Penney G. P., Tomaževič D., van Walsum T., Niessen W. J., *in Proc. MICCAI 2004*, C. Barillot, D. R. Haynor, and P. Hellier, eds., *3216*, **2004**, 574.
24. Herman G. T., Kuba A., eds., *Discrete Tomography: Foundations, Algorithms, and Applications*, Boston Birkhäuser, **1999**.
25. Natterer F., Wübbeling F., *Mathematical Methods in Image Reconstruction, Philadelphia, PA: Society for Industrial and Applied Mathematics*, **2001**.
26. Harauz G., Ottensmeyer F. P., *Ultramicroscopy*, **1984**, *12*, 309.
27. Provencher S. W., Vogel R. H., *Ultramicroscopy*, **1988**, *25*, 209.
28. Vogel R. H., Provencher S. W., *Ultramicroscopy*, **1988**, *25*, 223.
29. Dengler J., *Ultramicroscopy*, **1989**, *30*, 337.
30. Gelfand M. S., Goncharov A. B., *Transl. Math. Monographs*, **1990**, *81*, 97.

31. Goncharov A. B., *Transl. Math. Monographs*, **1990**, *81*, 67.
32. Penczek P., Radermacher M., Frank J., *Ultramicroscopy*, **1992**, *40*, 33.
33. Penczek P. A., Grassucci R. A., Frank J., *Ultramicroscopy*, **1994**, *53*, 251.
34. Radermacher M., *Ultramicroscopy*, **1994**, *53*, 121.
35. Penczek P. A., Zhu J., Frank J., *Ultramicroscopy*, **1996**, *63*, 205.
36. Lauren P. D., Nandhakumar N., *IEEE Trans. Pattern Anal. Machine Intell.*, **1997**, *19*, 417.
37. Grigorieff N., *J. Mol. Biol.*, **1998**, *277*, 1033.
38. van Heel M., Gowen B., Matadeen R., Orlova E. V., Finn R., Pape T., Cohen D., Stark H., Schmidt R., Schatz M., Patwardhan A., *Quart. Rev. Biophys.*, **2000**, *33*, 307.
39. Sorzano C. O. S., Jonić S., El-Bez C., Carazo J. M., De Carlo S., Thévenaz P., Unser M., *J. Struct. Biol.*, **2004**, *146*, 381.
40. Yang C., Ng E. G., Penczek P. A., *J. Struct. Biol.*, **2005**, *149*, 53.
41. Jonić S., Sorzano C. O. S., Thévenaz P., El-Bez C., De Carlo S., Unser M., *Ultramicroscopy*, **2005**, *103*, 303.
42. Czopf A., Brack C., Roth M., Schweikard A., *Periodica Polytechnica Ser. El. Eng.*, **1999**, *43*, 19.
43. Brown L. M. G., Boult T. E., *in IEEE Proc. MMBIA'96*, **1996**, 42.
44. Lemieux L., Jagoe R., Fish D. R., Kitchen N. D., Thomas D. G. T., *Med. Phys.*, **1994**, *21*, 1749.
45. Thévenaz P., Blu T., Unser M., *IEEE Trans. Med. Imag.*, **2000**, *19*, 739.
46. Unser M., Aldroubi A., Eden M., *IEEE Trans. Signal Processing*, **1993**, *41*, 821.
47. Unser M., Aldroubi A., Eden M., *IEEE Trans. Signal Processing*, **1993**, *41*, 834.
48. Penney G. P., Weese J., Little J. A., Desmedt P., Hill D. L. G., Hawkes D. J., *IEEE Trans. Med. Imag.*, **1998**,*17*, 586.
49. Press W., Flannery B., Teukolsky S., Vetterling W, *Numerical Recipes*, The Art of Scientific Computing, Cambridge University Press, **1988**.
50. Unser M., Aldroubi A., Eden M., *IEEE Trans. Pattern Anal. Machine Intell.*, **1993**, 15, 364.
51. Jonić S., Thévenaz P., Unser M., *in Proc. SPIE. Medical Imaging 2001: Image Processing*, M. Sonka and K. M. Hanson, eds., **2001**, *4322*, 1101.

52. Blu T., Thévenaz P., Unser M., IEEE Trans. Image Processing, **2001**, *10*, 1069.
53. Jonić S., Thévenaz P., Unser M., *in Proc. SPIE. Medical Imaging 2003: Image Processing*, M. Sonka and J. M. Fitzpatrick, eds., **2003**, 5032, 1049.
54. Hofstetter R., Slomczykowski M., Sati M., Nolte L. –P., *Comp. Aided Surg.*, **1999**, *4*, 65.
55. Henderson R., Baldwin J. M., Ceska T. A., Zemlin F., Beckmann E., Downing K. H., *J. Mol. Biol.*, **1990**, *213*, 899.
56. Velázquez-Muriel J. A., Sorzano C. O. S., Fernández J. J., Carazo J. M., *Ultramicroscopy*, **2003**, *96*, 17.